Simulation of noise generation and propagation caused by the turbulent flow around bluff bodies

Zamotin Kirill

e-mail: kirart@gmail.com*, icq: 209588862*

Summary

Accurate predictions of noise generation and spread in turbulent separating flows require detailed simulations of such flows to be performed. In this report CFD simulations of the unsteady turbulent flow field behind two outside side-view vehicle mirror models are presented and analyzed. The objective of this study are: to investigate numerically the transient flow structure around the mirror models in a range of incident flow velocities, to interpret the experimental observations available, to validate the CFD tools Ansys CFX 10.0 and Ansys Fluent 6.3, and to identify computational requirements and predictive capabilities for a range of turbulence modelling approaches.

In the simulations, qualitatively different flow behavior and vortical structure has been demonstrated for two mirror models considered in agreement with the suggestions earlier made based on the measured data. Surface pressure distributions and velocity fields as well as their fluctuation spectra are compared to the wind tunnel measurements provided by GM. Despite a discrepancy observed in the downwind region near the reflecting surface, a reasonable agreement was found. The performed simulations will provide a basis for subsequent aero-acoustic computations.

Statement of the problem

Two different full-scale mirror models were considered. The computational domain is shown on Figure 1.

In the nozzle outlet, a uniform mean velocity profile was assumed with turbulence intensity of $I = \sqrt{2k/3}/V = 0.01$, and integral length scale of $l_t = 0.7\ m$. The inlet turbulence is not felt to play an important role since the inlet is located rather far upstream of the mirror. This allows the correct turbulent structures to establish themselves before the incoming flow reaches the mirror model.

Quantitative estimates of turbulent flow characteristics are summarized in the Table 1 for a range of inlet flow velocities from 10 m/s to 50 m/s. In particular, integral scales (length, time, and velocity) are estimated against the Kolmogorov ones thereby demonstrating characteristic values for the fluctuation spectrum of fully developed turbulence.

Two mean flow velocities, 30 m/s and 40 m/s, have been considered at this phase of the work.

Table 1. Turbulent characteristics in airflow around mirror models[1]

Flow velocity V, m/s	Reynolds number, $Re = VL/\nu$	Integral scales			Kolmogorov scales			Turbulent kinetic energy (TKE), m²/s²	TKE dissipation rate, m²/s³	Turbulent Reynolds number
		Length, m	Time, s	Rms velocity fluctuation, m/s	Length, m	Time, s	Velocity, m/s			
		$l_t \approx 0.1L$	$\tau_t = \dfrac{l_t}{u'}$	$u' \approx 0.1V$	$\eta_K \propto \dfrac{l_t}{Re_t^{3/4}}$	$\tau_K = \left(\dfrac{\nu}{\varepsilon}\right)^{1/2}$	$u_K = (\varepsilon\nu)^{1/4}$	$k = \dfrac{3}{2}u'^2$	$\varepsilon = \dfrac{\nu^3}{\eta_K^4}$	$Re_t = \dfrac{u'l_t}{\nu}$
10	$0.93\cdot10^5$	$1.4\cdot10^{-2}$	$14\cdot10^{-3}$	1.0	$8.3\cdot10^{-5}$	$4.6\cdot10^{-4}$	0.18	1.5	$7.1\cdot10^2$	$0.9\cdot10^3$
20	$1.9\cdot10^5$	$1.4\cdot10^{-2}$	$7.0\cdot10^{-3}$	2.0	$4.9\cdot10^{-5}$	$1.6\cdot10^{-4}$	0.30	6.0	$5.7\cdot10^2$	$1.9\cdot10^3$
30	$2.8\cdot10^5$	$1.4\cdot10^{-2}$	$5.0\cdot10^{-3}$	3.0	$3.6\cdot10^{-5}$	$8.8\cdot10^{-5}$	0.41	13.5	$1.9\cdot10^3$	$2.8\cdot10^3$
40	$3.7\cdot10^5$	$1.4\cdot10^{-2}$	$3.5\cdot10^{-3}$	4.0	$2.9\cdot10^{-5}$	$5.7\cdot10^{-5}$	0.53	24.0	$4.6\cdot10^3$	$3.7\cdot10^3$
50	$4.7\cdot10^5$	$1.4\cdot10^{-2}$	$2.8\cdot10^{-3}$	5.0	$2.5\cdot10^{-5}$	$4.1\cdot10^{-5}$	0.60	37.5	$8.9\cdot10^3$	$4.7\cdot10^3$

[1] Characteristic length is $L = 0.14$ m.

Flow equations

To simulate the flow, the Navier-Stokes system that includes continuity and momentum equations is solved

$$\frac{\partial \rho}{\partial t} + \frac{\partial \rho u_j}{\partial x_j} = 0,$$

$$\frac{\partial \rho u_i}{\partial t} + \frac{\partial \rho u_j u_i}{\partial x_j} = -\frac{\partial p}{\partial x_i} + \frac{\partial \tau_{ij}}{\partial x_j}.$$

Both classical Reynolds averaged Navier-Stokes (RANS) approach and its combination with Large-Eddy Simulation (LES) that is referred as Detached Eddy Simulation (DES) methodology have been exploited in this study. When equations (1) and (2) are treated as averaged (RANS) or filtered (LES), the stress tensor τ_{ij} is equal to that for a Newtonian fluid complemented by turbulent stresses, $-\rho \overline{u_i' u_j'}$:

$$\tau_{ij} = 2\mu S_{ij} - \frac{2}{3}\mu \frac{\partial u_k}{\partial x_k}\delta_{ij} - \rho \overline{u_i' u_j'}, \qquad S_{ij} = \frac{1}{2}\left(\frac{\partial u_i}{\partial x_j} + \frac{\partial u_j}{\partial x_i}\right)$$

Where $S_{ij} = \frac{1}{2}\left(\frac{\partial u_i}{\partial x_j} + \frac{\partial u_j}{\partial x_i}\right)$ is the strain-rate tensor.

Thus in equations mean or filtered values are implied instead of instantaneous quantities (overbars are omitted over the averaged or filtered variables). Within the eddy viscosity concept, turbulent stresses are expressed through the turbulent viscosity, μ_t, and the mean flow strain rate:

$$-\rho \overline{u_i' u_j'} = 2\mu_t S_{ij} - \frac{2}{3}\left(\mu_t \frac{\partial u_k}{\partial x_k} + \rho k\right)\delta_{ij},$$

where $k = \overline{u_i' u_i'}/2$, the turbulent kinetic energy (TKE), and, μ_t, the turbulent viscosity, are defined by a turbulence model. Flow is assumed to be incompressible ($\rho = \text{const}$) within the velocity range considered.

Computational grids

Multi-block computational grids used in the simulations were constructed with *Ansys ICEM CFD* 10.0. The computational domain was divided onto several sub-domains, each covered by a separate curvilinear structured grid. To assess grid dependency of the results, two grids with total number of control volumes of 2.92M (referred below as *coarse grid*) and 7.15M (*fine grid*) have been used.

Table 2. Characteristic sizes of grid elements in near wake downstream the mirror models

Computational grid	Kolmogorov length, 10^{-3} m	Integral length, 10^{-3} m	Characteristic element edge size, 10^{-3} m				Number of elements
			at two distances downstream the mirror model, longitudinal size		normal to top surface of the mirror model	normal to reflecting surface	
			0.1 m	0.5 m			
Coarse	$10^{-1} - 10^{-2}$	$10^{1} - 10^{2}$	10	10	10	3	2 915 946
Fine			2	10	3	1.5	7 151 942

Characteristic grid sizes are compared to turbulent length scales in Table 1.

Flow Results

Table surface pressure distributions

Adequate prediction of the surface pressure distributions is necessary for accurate simulations of noise originated from the dipole surface sources.

Comparison of the pressure distributions obtained with two grids is shown in Figure 2 for 30 m/s flow around MODEL A mirror model.

Mirror surface pressure distributions

Pronounced low-pressure region develops at the top of the model, which can inspire early flow separation. We have found indications of transient and multi-point separation and reattachment in this region. This can be seen in Figure 3 where several local and unsteady separation zones appear. Intensive fluctuations of pressure in this region have also been predicted. On that this region produces considerable amount of noise. Worth noting, appearance of multiple and unsteady separation zones has yet to be further investigated to ensure its physical, not numerical mechanism. It could be done by mesh refinement in the streamwise direction.

The sound propagation equation

The acoustic analogy is derived by rearrangement of the continuity and momentum equations,

$$\frac{\partial \rho}{\partial t} + \frac{\partial \rho u_j}{\partial x_j} = 0,$$

$$\frac{\partial \rho u_i}{\partial t} + \frac{\partial \rho u_j u_i}{\partial x_j} = -\frac{\partial T_{ij}}{\partial x_j} \quad \text{where} \quad T_{ij} = p\delta_{ij} - \tau_{ij}$$

is the stress tensor including pressure, p, and viscous stresses,

$$\tau_{ij} = \mu\left(\frac{\partial u_i}{\partial x_j} + \frac{\partial u_j}{\partial x_i}\right) - \frac{2}{3}\mu\frac{\partial u_k}{\partial x_k}\delta_{ij}$$

It is assumed that in a confined region, Ω, fluid flow field is known from this equations. Whilst the fluid (having pressure p_0 and density ρ_0) is at rest beyond Ω. The following equation can be derived

$$\frac{\partial^2 \rho}{\partial t^2} - \frac{\partial^2}{\partial x_i \partial x_j}\left(T_{ij} + \rho u_i u_j\right) = 0.$$

Subtracting $c_0^2\left(\partial^2 \rho / \partial x_i \partial x_i\right)$ from both sides of last equation yields

$$\frac{\partial^2 \rho}{\partial t^2} - c_0^2\frac{\partial^2 \rho}{\partial x_i \partial x_i} = \frac{\partial^2 \tilde{T}_{ij}}{\partial x_i \partial x_j} \tag{1}$$

where $\tilde{T}_{ij} = \left(p - c_0^2\rho\right)\delta_{ij} + \rho u_i u_j - \tau_{ij}$ is the Lighthill's tensor, and $c_0 = \sqrt{\gamma\frac{p_0}{\rho_0}}$ is the speed of sound in the quiescent fluid.

Equation (1) is similar to that of acoustic wave propagation, the right hand side appears to be the source of the acoustic perturbations. The Lighthill's analogy is therefore formulated as follows: density fluctuations in an arbitrarily moving real compressible fluid are the same as those in a uniform quiescent fluid subject to the imposed stresses as expressed by the right hand side of Eq. (1). Thus, in the Lighthill's acoustic analogy, the actual flow is replaced by the T_{ij} distribution produced by the actual flow. Then, Eq. (1) governs the sound propagation in a uniform acoustic medium at rest, subject to the T_{ij} forcing.

Equation for Lighthill's tensor can be further rearranged neglecting molecular viscosity and thermal conductivity. In the ideal isentropic fluid $\mu = 0$ and $p = c_0^2 p$ therefore the Lighthill's tensor is reduced to $\tilde{T}_{ij} = \rho u_i u_j$ where density is non-uniform due to the acoustic perturbations. However, in low-Mach number flows, it can be reasonably assumed that $\rho = \rho_0$, and Eq. (1) simplifies to

$$\frac{\partial^2 \rho}{\partial t^2} - c_0^2\frac{\partial^2 \rho}{\partial x_i \partial x_i} = \rho_0\frac{\partial^2 u_i u_j}{\partial x_i \partial x_j} \tag{2}$$

The latter can be treated as the equation of sound (i.e. density fluctuations) propagation in a quiescent media, and the right hand side of Eq. (2) is the expression for source of sound produced by the flow in the region Ω. Equation (2) is also valid for perturbed density, $\tilde{\rho} = \rho - \rho_0$

Solving Eq. (2) is possible after the flow field is determined in Ω. That allows the sound pressure, $\tilde{p} = c_0^2(\rho - \rho_0)$ to be obtained.

Solutions to the sound propagation equation

The solution of Eq. (2) is the convolution of the right hand side with the Green function,

$$\tilde{p}(x,t) = \frac{1}{4\pi c_0^2}\frac{\partial^2}{\partial x_i \partial x_j}\int_\Omega [T_{ij}]\frac{dy}{r} \tag{3}$$

where $r = |\mathbf{x} - \mathbf{y}|$ is the distance between the source point $\mathbf{y}$ and the observer position $\mathbf{x}$, and the square brackets indicate that the bracketed quantity is taken at the retarded time, $t - |\mathbf{x} - \mathbf{y}|/c_0$. If an observer at $\mathbf{x}$ is in the *far field* then terms of order of r^{-4} and r^{-5} can be neglected and Eq. (3) is rewritten as

$$\tilde{p}(x,t) = \frac{1}{4\pi c_0^4}\int_\Omega \frac{(x_i - y_i)(x_j - y_j)}{r^3}\frac{\partial^2 [T_{ij}]}{\partial t^2}dy \tag{4}$$

For a numerical implementation of Lighthill's analogy, the temporal formulation (4) is more appropriate than that in Eq. (3) which is based on the spatial derivatives of T_{ij}. Note, neither Eq. (3) no Eq. (4) consider the effects of solid walls.

To overcome the latter limitation, the solution to Eq. (2) was extended by Curle [8] to include the effects of *solid walls at rest*. He solved Eq. (2) thereby obtaining the Kirchhoff formula,

$$\rho(\mathbf{x},t) = \frac{1}{4\pi}\int_S \left\{ \frac{1}{r}\left[\frac{\partial \rho}{\partial \mathbf{n}}\right] + \frac{1}{r^2}\frac{\partial r}{\partial \mathbf{n}}[\rho] + \frac{1}{c_0 r}\frac{\partial r}{\partial \mathbf{n}}\left[\frac{\partial \rho}{\partial t}\right]\right\}d\mathbf{y} + \frac{1}{4\pi c_0^2}\int_\Omega \frac{\partial^2 [T_{ij}]}{\partial y_i \partial y_j}\frac{d\mathbf{y}}{r}$$

the equivalent and more convenient equation can be derived:

$$\tilde{\rho}(\mathbf{x},t) = \underbrace{\frac{1}{4\pi c_0^2}\int_S \frac{\partial}{\partial t}[\tilde{\rho}u_i n_i]\frac{d\mathbf{y}}{r}}_{monopole} - \underbrace{\frac{1}{4\pi c_0^2}\frac{\partial}{\partial x_i}\int_S (\tilde{\rho}u_i u_j + T_{ij})[n_j]\frac{d\mathbf{y}}{r}}_{dipole} + \underbrace{\frac{1}{4\pi c_0^2}\frac{\partial^2}{\partial x_i \partial x_j}\int_\Omega [\tilde{T}_{ij}]\frac{d\mathbf{y}}{r}}_{quadrupole}$$

Where T_{ij} is the stress tensor, and $\tilde{T}_{ij}$ is the Lighthill's tensor. Equation results in an important conclusion. Indeed, it shows that sound generation is determined by three contributing sources. The first integral represents *monopole* sources distributed over the surface *S*. The second one corresponds to *dipole* sources also distributed over the surface *S*. This term includes sound refraction and diffraction at the surface. Finally, the third integral represents the *quadrupole* sound emission in the region of Ω.

Note, the surface *S* can be either permeable or solid; if *S* is a solid immovable wall then $u_i u_j = 0$, and equation simplifies:

$$\tilde{\rho}(\mathbf{x},t) = -\frac{1}{4\pi c_0^2}\frac{\partial}{\partial x_i}\int_S [T_{ij}n_j]\frac{d\mathbf{y}}{r} + \frac{1}{4\pi c_0^2}\frac{\partial^2}{\partial x_i \partial x_j}\int_\Omega [\tilde{T}_{ij}]\frac{d\mathbf{y}}{r}$$

The above formulated Lighthill's analogy can now be extended: density fluctuations in an arbitrarily real compressible fluid moving inside the region Ω that contains solid walls are the same as those in a uniform quiescent fluid affected by the *dipoles* distributed over the wall *surface S* and the *quadrupoles* distributed in the *volume* of Ω.

Last equation can be simplified by neglecting effects of viscosity:

$$\tilde{\rho}(\mathbf{x},t) = -\frac{1}{4\pi c_0^2}\frac{\partial}{\partial x_i}\int_S [p]n_i \frac{d\mathbf{y}}{r} + \frac{1}{4\pi c_0^2}\frac{\partial^2}{\partial x_i \partial x_j}\int_\Omega \rho_0 [u_i u_j]\frac{d\mathbf{y}}{r}$$

Acoustic pressure and sound pressure level in air sensor locations

Acoustic pressures have been calculated and sound pressure level have been predicted for some cases: 30 m/s and 40m/s wind speed, coarse and fine grid. The analysis of results indicates that reasonable agreement between predicted and measured SPL has been obtained although the predicted ones are underestimated, particularly for frequencies greater
1 kHz.

Acoustic pressure and sound pressure level in surface microphone locations

Measured SPL frequency distributions are qualitatively different for the microphones located inside and outside the recirculating zone behind the mirror model. Signals recorded inside the recirculating zone are determined by pressure fluctuations at the table surface, whilst those recorded outside the recirculating zone are mainly due to the external noise.
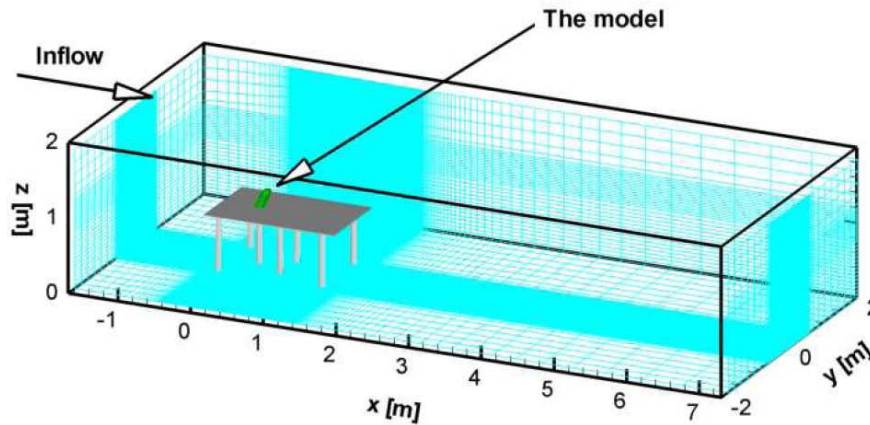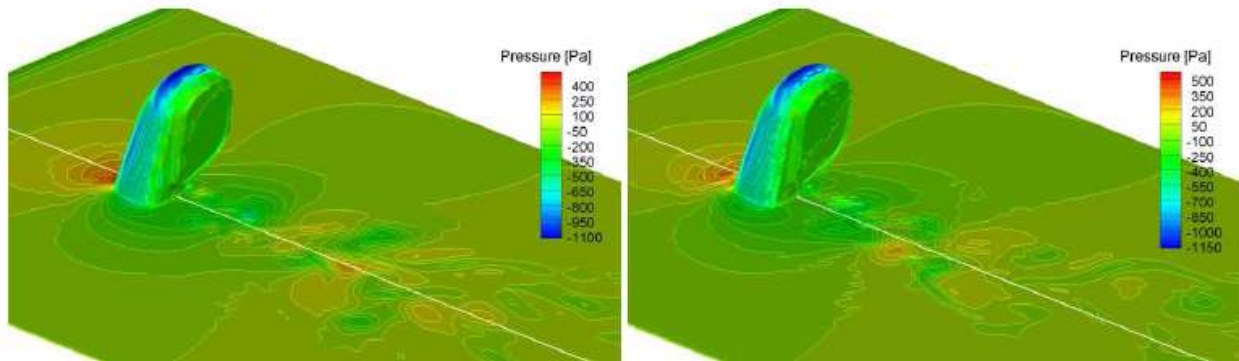

Figure 1. The computational domain

(a) Coarse grid   (b) Fine grid

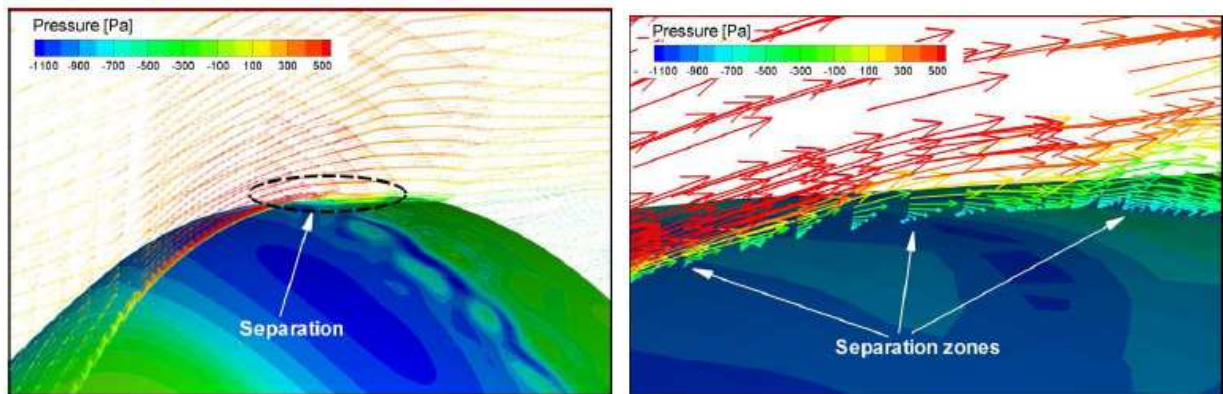**Figure 2**. Surface pressure resolution with two grids.

Figure 3. Early separation zone at the top of mirror. Velocity vectors colored by velocity magnitude